# Physics Results From Alpha Magnetic Spectrometer 1998 Shuttle Flight

*Proceeding of the 7-th Taiwan Astrophysics Workshop,*
*National Central University, Taiwan,*
*Oct. 18,2000*

M. A. Huang
*Institute of Physics, Academia Sinica, Taipei, 11529, Taiwan, R.O.C.*

## ABSTRACT

The Alpha Magnetic Spectrometer (AMS) is a particle detector designed to detect antimatter. During the 10-day test flight on the space shuttle in June 1998, AMS detected $10^8$ events. Upon analysis, no antimatter was found and the antimatter limit was reduced to $1.1 \times 10^{-6}$. The proton spectrum shows some differences with the cosmic ray flux used in atmospheric neutrino simulation. A large amount of protons, positrons, and electrons were found below the geomagnetic rigidity cutoff. The energy of these particles are as high as several GeV, one order of magnitude higher than any previously measured energy in radiation belts. These particles also exhibit many interesting features. This paper reviews the results in the four published papers of the AMS collaboration and provides explanation for some features of the albedo particles.

## 1. Introduction

The Alpha Magnetic Spectrometer is a space borne charged particle detector (Ahlen 1994) and will be installed on the International Space Station in 2003 for three years. Its aims are to detect the antimatter and dark matter, and to perform precision measurement of primary cosmic rays. In June 1998, the detector performed an engineering test run on board the space shuttle mission STS-91 for 10 days and recorded approximately $10^8$ events. The physics results had been analyzed and published. This review begins with a short introduction to the AMS. Section 2 describes the physics of charged particles in the geomagnetic field. The physics results from the AMS 1998 shuttle flight are presented in the rest of this paper. The final section summarizes all the results.

### 1.1. AMS physics goals

From our current understanding of elementary particle physics, energy always materializes to equal amount of matter and antimatter. If antimatters exist in the universe, then their existence could be detected by either indirect search using gamma ray line spectrum, which comes from the annihilation of antimatter and matter; or by the direct search using cosmic rays detector. On the other hand, if antimatters are absent in the universe, then CP-violation and baryon nonconservation must be observed. However, all such searches have been negative (references 1-7 of Alcaraz 1999). There are no positive evidences supporting the existence or absence of antimatter. A direct detection of anti-nuclei such as anti-helium or anti-carbon could signal the existence of antimatter. The AMS is an accurate, large acceptance magnetic spectrometer, which will be installed on the International Space Station for three years. The large acceptance and long duration will reduce the anti-helium limit to $10^{-9}$.

Dark matter is another unsolved puzzle of the universe. One of the candidates of dark matter, WIMP (Weakly Interacting Massive Particle), could annihilate in the halo of galaxy and produce an excess of positrons (Hardung & Ra-

maty 1987; Aharonian & Atoyan 1991; Dogiel & Sharov 1990; Tylka 1989; Turner & Wilczek 1990; Kamionkowski & Turner 1991). The AMS can make indirect search of WIMP through the detection of positrons.

The majority of particles detected by the AMS are cosmic rays. The large acceptance and multiple sub-detectors of AMS can make precise measurements of cosmic rays flux and composition. These data are useful for studies on cosmic rays and atmospheric neutrino simulation (Honda et al. 1995, Gaisser 1999).

### 1.2. AMS01 space shuttle flight

The AMS collaboration consists of 32 institutions from 13 nations[1]. In June 1998, a prototype detector, called AMS01, was flown in space shuttle Discovery on flight STS-91. During this 10-day test flight, AMS01 gathered approximately $10^8$ events. The various components of the AMS are listed in Table 1 and shown in Figure 1. The notation of the coordinate system is as follows. $\widehat{x}$ is the magnetic field direction, non-bending direction; $\widehat{y}$ is the bending direction, and $\widehat{z}$ is the cylindrical axis.

## 2. Introduction to physics of charged particles in the geomagnetic field

Since cosmic rays are charged particles, their trajectories are bent by the magnetic field. The geomagnetic field affects the arrival directions of cosmic rays, blocks lower energy cosmic rays, and traps some low energy particles in radiation belts.

### 2.1. Geomagnetic field

The geomagnetic field consists of two parts, the internal field (main field) produced by magnetic moments of the Earth and the external field driven by the solar wind plasma. The internal and external fields merge at distance $> 10R_E$, where $R_E$ is the mean earth radius 6371.2 km, forming the magnetosphere. Although the AMS flight was at low altitude of 380km, the magnetic field lines

[1]Three institutions from Taiwan participated in this project. The Chung Shan Institute of Science and Technology designed and manufactured the electronics boards, while the Academia Sinica and National Central University were involved in data acquisition system and data analysis.

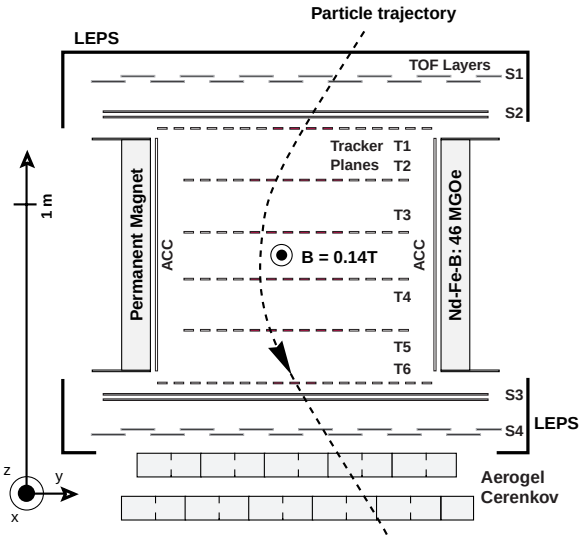


Fig. 1.— Schematic view of the AMS01 detector.

passing through the AMS path can reach an altitude of approximately 6.4 $R_E$, well inside the magnetosphere. Therefore, only the internal field is considered in the AMS physics analysis.

Although the main field can be simplified as a dipole field, the error could be as big as 30% in some regions. In realistic field, a series of spherical harmonics were used to fit to the measured value.

$$V = R_E \sum_{n=0}^{\infty} (\frac{R_E}{r})^{n+1} \sum_{m=0}^{n} P_n^m(\cos\theta) \times (g_n^m \cos m\phi + h_n^m \sin m\phi)$$

Where the $P_n^m(\cos\theta)$ is the associated Legendre function with Schmidt normalization of the degree n and order m. $g_n^m$ and $h_n^m$ are Gaussian coefficients determined by the magnetic field. The coefficient $n = 1$ corresponds to the dipole term.

Every five years since 1945, the International Geophysics Union publishes the fitted coefficients to the 10th degree. This field model is called the International Geomagnetic Reference Field (IGRF). Also, the US Department of Defense fits the coefficients to the 12th degree, this field model is called the World Magnetic Model (WMM). Those two models are slightly different (Huang 2001) and their details can be found on the web[2].

[2]http://nssdc.gsfc.nasa.gov/space/model/ and

TABLE 1
THE COMPONENTS OF THE AMS01 DETECTOR AND THEIR PROPERTIES.

| Components | Descriptions |
|---|---|
| Magnet | 1.9 tons of Nd-Fe-B permanent magnet,<br>Inner radius 1115 mm, length 800mm,<br>Dipole field perpendicular to cylindrical axis,<br>Analyzing power $BL^2 = 0.14 Tm^2$. |
| Tracker | 6 planes double-side silicone tracker,<br>resolution in bending direction $\sigma_y = 20\mu m$,<br>non-bending direction $\sigma_x = 33\mu m$,<br>Measure rigidity and charge. |
| Time of Flight (TOF) | 4 planes plastic scintillators, two above magnet, two under magnet.<br>Resolution 120psec<br>Measure velocity and charge |
| Aerogel Cherenkov counter | Refractive index 1.035<br>Separation of leptons/hadrons at energy $< 1$ GeV |
| Anticoincidence counter | Plastic scintillators surrounding the inner surface of magnet.<br>Veto the events penetrating into magnet or interacting in the magnet. |
| Low energy particle shield | Carbon fiber 6 mm thick, density 1.3gm/cm$^3$<br>Shield from low energy particles |
| AMS01 flight | Inclination angle 51.7°<br>Altitude 350 to 390km<br>Data taking time: 184 hours |

Along the west coast of South America and southern Atlantic Ocean, the magnetic field is the weakest on the Earth surface. Because of high radiations, many satellites experience some troubles when flying over these regions. The phenomenon in this region is known as the *"South Atlantic Anomaly"* (SAA). Because of high deadtime when the AMS flies through the SAA, the data taken in the SAA are excluded in the data analysis.

For magnetic coordinates, the dipole coordinates were relative to the dipole axis. In realistic field, Corrected GeoMagnetic coordinates (CGM, Gustafsson 1992) were commonly used by space scientists and geophysicists. The 0° of CGM longitude passes through the SAA area, north and south magnetic poles. Figure 2 shows the contour line of magnetic field strength and the CGM coordinates at the Earth surface. The notation of magnetic latitude used in AMS publications is $\theta_m$. To avoid confusion with the zenith angle and to be consistent with common practice, $\lambda_m$ is used in this paper. The symbol of magnetic longitude is $\phi_m$.

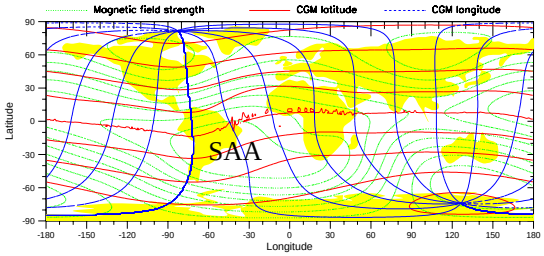


Fig. 2.— The magnetic field and coordinates used in AMS01. The dotted contour lines are the magnetic field strength at the Earth surface, and the solid/dash lines are the magnetic latitude/longitude. The South Atlantic Anomaly region is marked in this figure.

## 2.2. Rigidity cutoff

The geomagnetic field shields the Earth from cosmic rays bombardment. Below a threshold, the rigidity cutoff, the cosmic rays cannot penetrate through the geomagnetic field into the lower atmosphere. Also particles with rigidity below the threshold cannot escape from the geomagnetic field, i.e. particles are trapped by the geomagnetic field. In dipole field, the rigidity cutoff can be expressed in analytical form, called Strömer cutoff (Strömer 1930):

$$R_{cutoff} = \frac{M \cos^4 \lambda}{r^2(1+\sqrt{1-\cos\alpha\cos^3\lambda})^2}$$

$$R_{cutoff} = \frac{59.6\ \cos^4\lambda\ (GV/c)}{(r/R_E)^2(1+\sqrt{1-\cos\gamma\cos^3\lambda})^2} \quad (1)$$

$M$: Dipole moment;
$\lambda$: Magnetic latitude;
$r$: Radial distance;
$\gamma$: Incident angle from the west.

In realistic field, the cutoff cannot be formulated as a simple formula. The cutoff becomes a band of intermittent transition, which is called penumbra. Numerical calculation is needed to study the cutoff in realistic field. Figure 3 shows the vertical cutoff, $\gamma = 90°$ at altitude of 40 km.

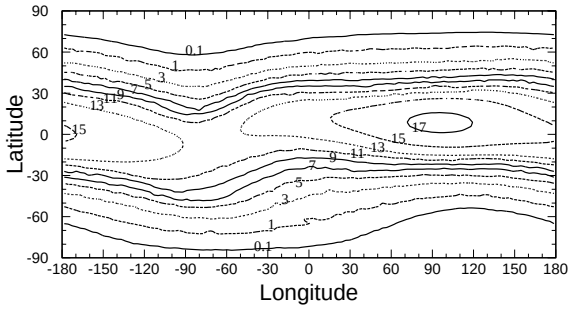


Fig. 3.— The rigidity cutoff in GV/c of normal incident at altitude of 40km.

## 2.3. Motions of trapped particles in geomagnetic field

For particles trapped inside the geomagnetic field, there are three types of motions (Walt 1994). They are the gyrations along a guiding center magnetic field line, the north-south bounce motions due to the repelling force of convergent magnetic fields, and the east-west drift motions due to gradient drift and curvature drift. The positive charged particles drift eastward while the negative charged particles drift westward.

http://www.ngdc.noaa.gov/seg/potfld/magmodel.shtml

## 3. Search for antihelium

### 3.1. Resolution

After the AMS01 flight, the detector was re-examined, first using the heavy ion (He,C) beam from 1.0 to 5.6 GV in GSI-Darmstadt, and then using the proton and pion beam 2 to 14 GV in CERN. The performance of the detector remained the same before, during, and after the flight (Alcaraz 1999).

At 2 to 10GV, the resolution is approximately 0.11- 0.14. At lower rigidity, the resolution becomes worse due to scattering, while at higher rigidity, the resolution deteriorates due to limited resolution of silicon tracker.

### 3.2. Data selection

Major contaminations of antihelium are confusions of charge magnitude $|z|$ and charge sign. The probability of confusion of $|z| = 2$ from $|z| = 1$ was estimated to be less than $10^{-}7$ by the measurements of $z^2$ from the TOF and tracker. Particle directions are determined by the TOF. The large-angle nuclear scattering events were identified and excluded by the large error or asymmetry of rigidity. The asymmetry $A_{12}$ is the relative error of rigidity of first half track $R_1$ and last half track $R_2$, where $A_{12} = (R_1 - R_2)/(R_1 + R_2)$. In addition, events with collinear delta rays were rejected by identifying excess of energy within 5mm of the track. Finally, a probabilistic function was constructed from measurements of velocity, rigidity, and energy loss which described the compatibility of these measurements with passage of helium or antihelium.

### 3.3. Antimatter search result

The last four candidates fail to be compatible with antihelium, and $2.86 \times 10^6$ helium with rigidity of 1 to 140GV survives all the cuts. The antimatter limits at 95% confidence level are then estimated by the following three methods. (1) Assuming that antihelium has the same spectrum as helium, an assumption commonly used in many antimatter experiments, the $\overline{\mathrm{He}}/\mathrm{He} = 1.1 \times 10^{-6}$ in the rigidity range of 1 to 140 GV. This result and some previous limits are plotted in Figure 4. (2) Assuming uniform $\overline{\mathrm{He}}$ rigidity spectrum, the $\overline{\mathrm{He}}/\mathrm{He} = 1.8 \times 10^{-6}$ at 1.6 to 40GV and $3.9 \times 10^{-6}$ at 1.6 to 100 GV. (3) For a conservative upper limit, which is independent of the $\overline{\mathrm{He}}$ spectrum, the $\overline{\mathrm{He}}$ limit is a function of rigidity (Fig. 9 of Alcaraz 1999).

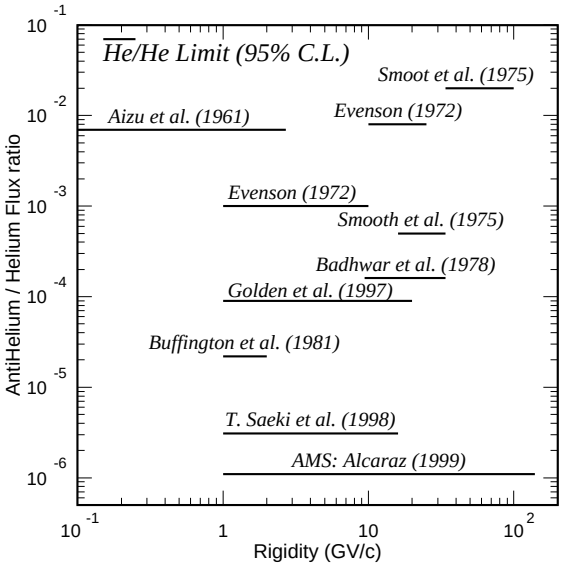


Fig. 4.— The AMS antihelium limit is plotted with some previous measurements. This limit assumes that antihelium has the same spectrum as helium.

## 4. Proton spectrum

Although the primary cosmic ray flux has been measured many times, the AMS is the first instrument that measures cosmic rays globally. This information is essential to the atmospheric neutrino calculation.

### 4.1. Proton spectrum

In this study (Alcaraz 2000A), the acceptance was restricted to events with incident angle within 32° from the $\hat{z}$ axis, the cylindrical axis of the AMS01 magnet. Two periods of data were used. For the first period, the $\hat{z}$ axis points to 1° around the zenith. Data taken in this period are referred to as *"downward"* going. For the second period, the $\hat{z}$ axis points to 1° around the nadir. Data taken in this period are referred to as *"upward"* going.

The major contaminations of proton are charged pions and deuterons. The pions are produced in the top part of the AMS. They account for 5% at below 0.5 GeV and decrease rapidly at higher energy. The deuterons abundance is about 2% in cosmic rays. Both pions and deuterons can be rejected by requiring the measured mass to be consistent with mass of proton within three sigmas. Owing to the detector resolution and possible energy loss in detector materials, the measured spectrum need to be unfolded to get the incident spectrum. This procedure uses detector resolution from Monte-Carlo simulation and Bayes theorem (reference 7,8 of Alcaraz 2000A). Figure 5 shows the differential spectrum of several magnetic latitude intervals.

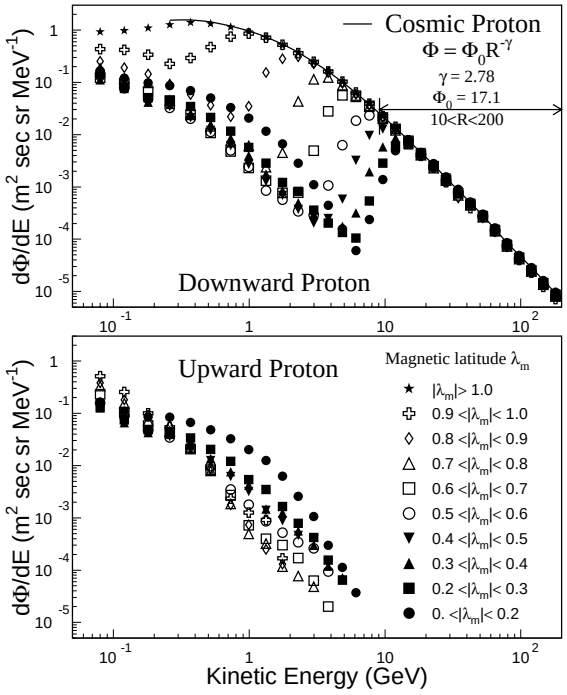


Fig. 5.— The upper figure shows the downward proton fluxes in 10 latitude intervals. The solid line is the cosmic proton. For each latitude interval, the proton fluxes have a dip due to the rigidity cutoff; below this cutoff, there is a second spectrum. The lower figure shows the upward proton fluxes. Cosmic rays do not exist in these upward events.

For downward events, the outer envelop is the cosmic ray flux. The proton fluxes decrease rapidly in some regions because of the geomagnetic rigidity cutoff. However, the proton fluxes rise again at energy lower than the cutoff. For upward events, all the protons are below the cutoff. Those spectra below cutoff are referred to as *"second spectra"*. Since the radiation belts are at altitude over 1000km, such large second fluxes are not expected at the AMS altitude of around 380km. These second spectra are discussed in detail in Section 6.

### 4.2. Cosmic proton spectrum

For primary cosmic ray proton, all the available data are used in a separate study (Alcaraz 2000C). The data were collected in three periods in which the AMS $\widehat{z}$ axis pointed to 0°, 20°, 45° around the zenith. The acceptance of AMS was extended to 38° from the $\widehat{z}$ axis of AMS. The cosmic proton must have rigidity R, such that $R > R_c \times (1.2 + 2\sigma(R_c))$ where $R_c$ is the maximum rigidity cutoff of all incident angles and $\sigma(R_c)$ is the uncertainty of rigidity at $R_c$. The acceptance of AMS is $0.15 m^2 sr$ on average and only weakly dependent on momentum. The background rejection and spectrum unfolding are the same as described in the previous section.

The systematic errors were studied in detail in this study. The first source of systematic error was the variation in trigger efficiency and reconstruction accuracy. The total error from this origin is 3.5%. The second source of systematic error came from Monte Carlo corrections. This source contributes 3% in total. The third source of systematic error came from the unfolding procedures, they are typically 1% below 20GeV and reach 5% at 100GeV. The final spectrum is fitted to the power law spectrum at rigidity $10 < R < 100$ GV.

$$d\phi/dR = \phi_0 \times R^{-\gamma} \qquad (2)$$

The differential spectrum index $\gamma$ is $2.78 \pm 0.009(\text{fit}) \pm 0.019(\text{sys})$ and the normalization constant $\phi_0$ is $17.1 \pm 0.15(\text{fit}) \pm 1.3(\text{sys}) \pm 1.5(\gamma)$ $\text{GV}^{2.78}/(\text{m}^2\text{srMeV})$. Figure 6 shows the above result and several recent measurements and spectrum used in the atmospheric neutrino calculation model. The AMS spectrum is consistent with that of previous measurements; however, the HKKM model (Honda 1995) seems to have higher flux at energy above 20 GeV.

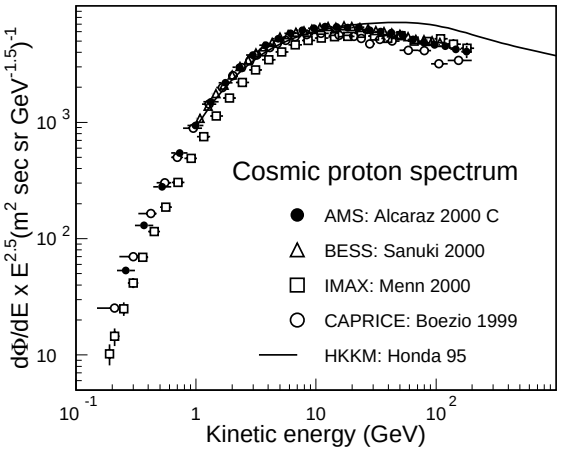


Fig. 6.— The cosmic proton fluxes measured by the AMS are plotted with some previous measurements. The solid line is the primary proton flux used in the HKKM atmospheric neutrino model.

## 5. Leptons

### 5.1. Events selection and contamination

To study electrons and positrons (Alcaraz 2000B), the track must pass through the aerogel Chrenkov counter; therefore the acceptance was limited to 25° from the $\widehat{z}$ axis. All four periods of shuttle attitude, 0°, 20°, 45°, and 180° from the zenith, are included. The electron candidates are selected with charge -1, velocity compatible with speed of light. The major backgrounds are protons with wrongly measured rigidity and pions produced in detector materials. These two backgrounds are removed by $\chi^2$ of trajectory fitting and number of hits near reconstructed track. After this cut, the chance of a proton being misidentified as an electron is in the order of $10^{-4}$. The effective energy range for electron is 0.2 to 40GeV. The positron candidates are selected with charge +1, velocity compatible with speed of light. The major background is proton with poorly reconstructed velocity. Above 1 GeV, the protons are rejected by requiring the two measurements at two separate Chrenkov counter layers to be compatible with those of positrons. Lower energy protons are rejected by requiring velocity measurement in TOF and tracker to be compatible with that of positrons. Owing to the under-performance of aerogel counter, the effective energy range for positron is only 0.2 to 3 GeV.

### 5.2. Spectrum

The conversion from number of events to spectrum is similar to the process used in obtaining the proton spectrum. Figure 7 shows the electron and positron spectra at several magnetic latitude intervals. Similar to the proton spectrum, primary cosmic rays exist at high energy and the second spectrum appears below the rigidity cutoff.

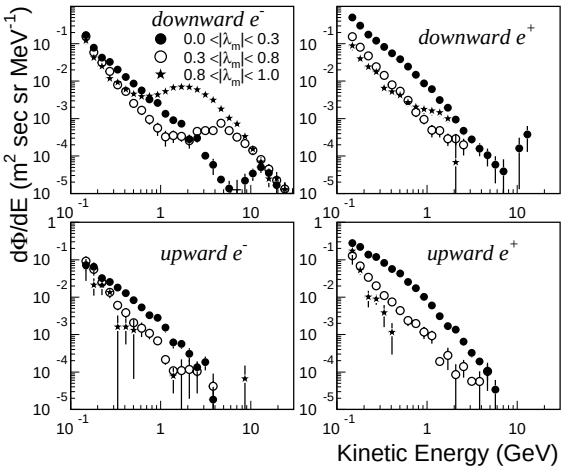


Fig. 7.— The electron and positron fluxes measured by the AMS are plotted in three latitude intervals.

Figure 8 shows the cosmic positron fraction, $e^+/(e^+ + e^-)$. The results are consistent with most previous measurements. With the current detector, the AMS01 cannot identify the possible positron signal from annihilation of WIMP at higher energy. The new AMS detector for 2003 will add ring imaging Chrenkov detector and calorimeter and should have better chance to detect this dark matter signal.

## 6. Albedo Particles

This section contains the preliminary results from the study of the particles below the cutoff by the author. The discussion is purely the author's opinion, **NOT** that of the AMS collaboration.

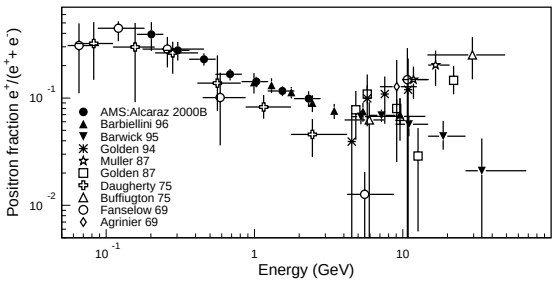


Fig. 8.— The positron fraction of primary cosmic rays measured by the AMS and some previous measurements. At energy $< 3$ GeV, the AMS and CAPRICE (Barbiellini 1996) show consistent results.

### 6.1. Introduction

Below the geomagnetic cutoff, charged particles cannot escape from the confinement of the geomagnetic field. Trapped particles in radiation belts have the lowest altitude above the atmosphere; they could exist for a long time, which is much longer than the drift period. Particles with the lowest altitude inside the atmosphere will be absorbed in a short time. Particles below the rigidity cutoff are observed in all areas covered by the AMS and all the particles studied so far include proton, electron, positron and helium. These particles, known as albedo particles, are found to originate from the atmosphere and rebound to space. The albedo particles had been previously detected by many balloon experiments (Bleeker 1965). The splash albedo and re-entrant albedo were part of background of cosmic ray antiparticle measurements. Most of the radiation belts experiments in the 60s and 70s could not distinguish between electrons from positrons. However, the presence of positrons in the radiation belts had been reported as early as 1983 (Just 1983, Galper 1983).

The balloon experiments are mostly conducted in high latitudes and their operations were short, from several hours to several days. Although the space instruments have longer operation time, their detectors are much smaller than the balloon instruments, therefore with smaller acceptance. The AMS combines the advantage of these two types of experiments, a large acceptance and long duration flight. The AMS also performs measurements at lower latitude and covers 78% of the Earth surface. These factors make AMS a better tool for studing albedo particles in detail. AMS also make measurements at higher energy ($\sim$ GeV), almost one order of magnitude higher than that in previous radiation belts experiments.

Figure 9 shows the AMS results and some previous measurements. Only the AMS measurements are shown with error bars, while others are shown without. The albedo electron fluxes are quite consistent with those of other results. However, variations among the different measurements are around one order of magnitude. The reason behind this large difference is still unknown; it may be due to the effect of the geomagnetic field, change in primary cosmic rays fluxes, or some other systematic effects.

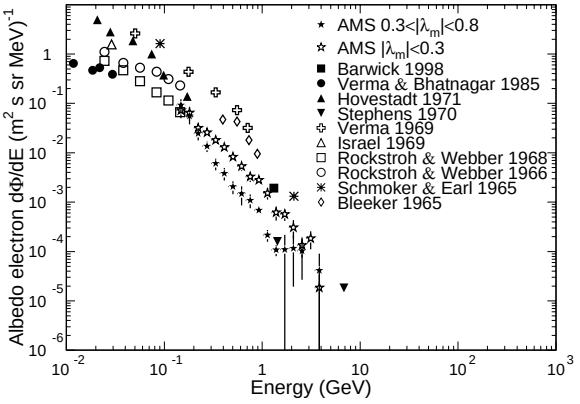


Fig. 9.— The AMS upward going electrons consist only of albedo particles (Alcaraz 2000B). The flux of low latitude, $|\lambda_m| < 0.3$, and mid latitude, $0.3 < |\lambda_m| < 0.8$ are shown here with some previous measurements.

The positron and anti-proton can be produced in the atmosphere and rebound to space. These particles could be confused with the cosmic rays. Their trajectories can be used to distinguish their source. We use a trajectory tracing program (Huang 2001) to calculate their past and future trajectories. This program uses the Runge-Kuta 4-th order integrator to solve the Lorentz equation. The particles are traced backward in time until they exit the geomagnetic field, (altitude $> 10R_E$), hit the ground, or exceed a pre-determined

time limit (typically 10 seconds). Particles coming from outside the geomagnetic field are cosmic rays, and have rigidity above the cutoff value. Those particles which hit the ground when traced backward are referred to as albedo particles. The positions where they come from (hit 40 km altitude or pass $10R_E$) are called the source. The positions where they stop (hit 40 km altitude or pass $10R_E$) are called the sink. The time from source to sink is defined as the flight time.

Events can be separated into five types according to their source and sink. The cosmic rays come from space and sink to the atmosphere. The albedo particles come from the atmosphere. Some cosmic rays enter the AMS altitude, and are then go back to space; they are cosmic rays but reflected back to space by the geomagnetic field. Some albedo events have rigidity above the cutoff and could exceed the $10R_E$ limit in forward tracing. These escaped albedo events are found in high latitude region where the cutoff values are low. Figure 10 shows the trajectory of these four types of events. For the trapped radiations, the particle must remain inside altitude 100km to $10R_E$ for over 20 seconds.

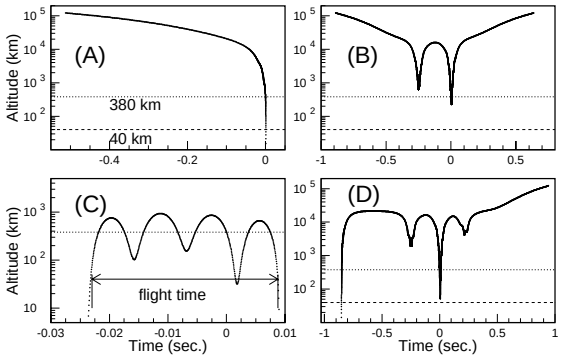


Fig. 10.— The time profile of radial distance of four types of events. (A) cosmic rays, (B) reflected cosmic rays, (C) trapped albedo, and (D) escaped albedo. Negative time means that the particle is traced backward in time, while positive time means that the particle is traced forward in time. The 380 km is the mean altitude at the detection site. The 40 km is used to define the flight time as shown in (C)

We traced all the electrons/positrons and protons below 6 GeV. They all have similar distributions. Most of these particles are either cosmic rays of trapped albedo particles, few are reflected cosmic rays or escaped albedo. No trapped radiation is observed within the AMS altitude and acceptance. However, trapped radiation is not totally ruled out, because the AMS does not cover the near horizon events.

### 6.2. Origin of albedo particles

At 1 MeV, the neutron could travel $37R_E$ during its lifetime. The decay products, protons and electrons, have few chances to exist inside $10R_E$. The cosmic ray albedo neutron decay, CRAND, could not account for the high energy albedo particles seen by the AMS. The source of albedo particles must be distributed globally and capable of producing positrons in large amount and continuously. The most possible mechanism behind the global production of positrons is the interaction of primary cosmic rays with atmospheric nucleus.

$$\text{H, He, ...} + \text{N}_2\ ,\ \text{O}_2\ ,\ ... \rightarrow\ \text{H} \,/\, \pi^{0,\pm} \,/\, K^{0,\pm} + ...$$
$$\pi^{0,\pm}\ ,\ K^{0,\pm} \rightarrow e^+\ ,\ e^- + ...$$

Under some special conditions, these secondary protons, electrons, and positrons move upward and become the albedo particles, some could move to the AMS altitude and be detected.

### 6.3. Flight time

Since these albedo particles are below the cutoff, their motions follow a pattern similar to that of trapped radiations. The bouncing times $N_b$ and drift times $N_d$ can be defined by

$$\begin{aligned} N_b &= \mathrm{T}/\tau_b \\ \tau_b &= 0.117[1 - 0.4635(\sin\alpha_{eq})^{3/4}](L/\beta) \\ N_d &= \mathrm{T}/\tau_d \\ \tau_d &= C_d[1 - 0.333(\sin\alpha_{eq})^{0.62}]/(L\gamma\beta^2) \\ C_d &= 1.557 \times 10^4 \ \text{ for electrons, positrons} \\ &= 8.841 \ \text{ for protons} \end{aligned} \tag{3}$$

where T is flight time, $L$ is the L-shell number, $\gamma$ is realistic factor , $\beta$ is velocity, and $\alpha_{eq}$ is the pitch angle at the magnetic equator. Note that $\tau_b$ and $\tau_d$ are approximation forms in dipole field and accurate to 0.5% (Walt 94). When the particle rigidity is close to the cutoff, the trajectory becomes irregular and these approximation formulas could have larger error.

Figure 11 shows the $N_b$ and $N_d$ distributions of electrons. The two horizontal bands are the events that have flight-time $\sim 1/2\tau_b$ or $\tau_b$, referred to as short flight-time (SFT) particles. The two vertical bands are the events that have flight-time $\lesssim \tau_d$, referred to as long flight-time (LFT) particles. The

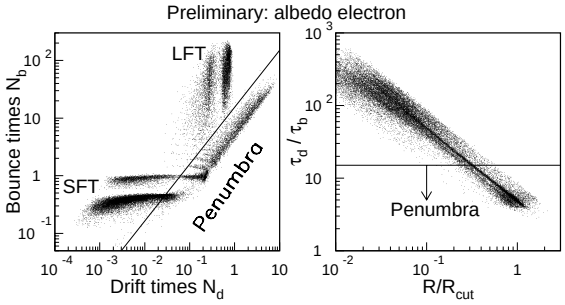


Fig. 11.— The left figure shows the distribution of bouncing times and drift times. The right figure shows the relation of the $\tau_d/\tau_b$ and ratio of rigidity ($R$) and cutoff ($R_{cut}$). When the rigidity inside the penumbra region $R/R_{cut} \sim 1$, the trajectory becomes irregular. The cut $\tau_d/\tau_b > 15$ is shown by the solid line.

diagonal band shows the events with $\tau_d/\tau_b < 15$, referred to as penumbra events, with rigidity inside the penumbra. Because of the momentum error, their origin cannot be determined precisely. Section 6.7 will discuss the penumbra events in detail. Albedo events are selected with $\tau_d/\tau_b > 15$ to avoid contamination from primary cosmic rays. Figure 12 shows the $N_b$ and $N_d$ distributions of albedo events.

In Fig. 6 of (Alcaraz 2000B), the flight time of LFT particles seems to be inversely proportional to kinetic energy. This is because $\tau_d$ is proportional to $1/\gamma\beta \simeq 1/\gamma$. The flight time of SFT particles seems to be independent of kinetic energy and forms two horizontal bands. The reason is that $\tau_b$ is proportional to $1/\beta$. For e+,e- at low latitude, the pitch angel at the magnetic equator does not change too much and $\beta \simeq 1$, therefore the flight time remains constant for different kinetic energy. If events from all latitudes are included, the two bands will be smeared and connected (Fig. 7 of Huangmh 2000). For the albedo protons, $\beta$ changes with kinetic energy. Therefore, the flight time is not the best indicator for classi-

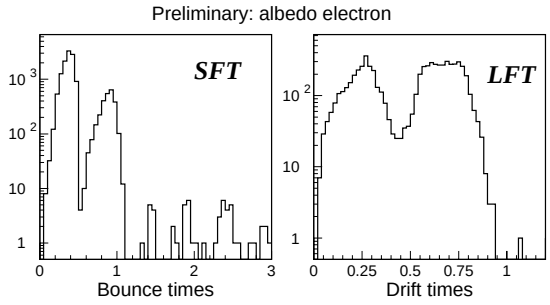


Fig. 12.— The left figure shows the distribution of bouncing times of SFT albedo positrons. The right figure shows the distribution of drifting times of LFT albedo positrons. Albedo electrons and protons have similar distributions.

fying the two groups; instead, $N_b$ can distinguish clearly SFT and LFT particles of different mass and latitude. In this study, $N_b < 3$ indicates SFT particles, and $N_b \geq 3$ indicates LFT particles.

Figure 13 shows the flight time distribution of electrons and positrons. The albedo events clearly show a two-peak structure, which correspond to SFT and LFT, respectively. The separation point is around 0.3 second. The albedo proton has a similar two-peak distribution but different separation time.

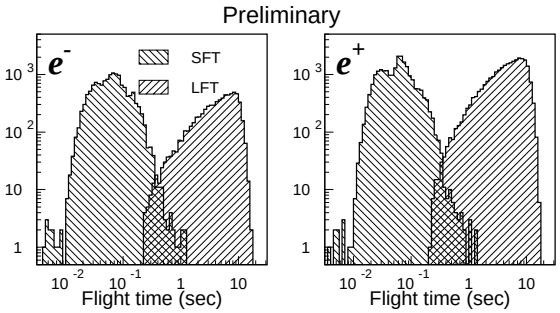


Fig. 13.— The flight time distributions of albedo electrons (left figure) and positrons (right figure), which have $\tau_d/\tau_b > 15$..

### 6.4. Comparison with radiation belts

The major differences between the albedo particles and trapped radiations are mirroring altitude

and life time outside the atmosphere. The mirroring altitudes of albedo particles are inside the atmosphere. Therefore, the life time is in the order of bounce period for SFT or drift period for LFT. The mirroring altitudes of trapped radiations are well above the atmosphere. Therefore, the trapped radiations can survive for a long time $\gg \tau_d$.

Despite these two differences, the albedo particles and trapped radiations share some common features, such as trajectory shape and spatial coverage. Figure 14 shows the distribution of L-shell of SFT and LFT electrons. The SFT particles covers L-shell up to L=6.4, where the outer radiation belt is. Most of the LFT particles cover L-shell in L=2, where the inner radiation belt is. It is clearly seen that these high energy albedo particles cover similar space as trapped radiations. *The radiation belts consist of not only trapped particles but also high energy secondary albedo particles.* Since these albedo particles not only gyrate around the AMS altitude, but also move to higher altitude. *It is misleading to call these particles "a ring of particle around 380km" or the third radiation belt.*

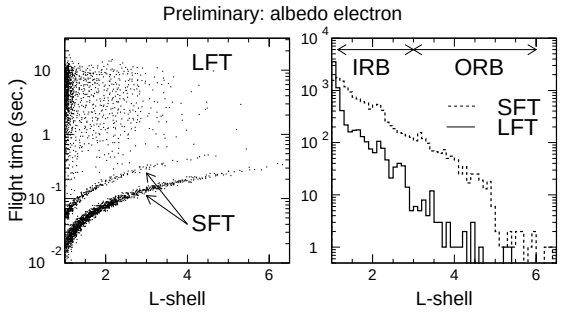


Fig. 14.— The left figure shows the distribution of flight time as a function of L-shell. The right figure shows spatial coverage of albedo particles. The LFT particles cover mainly in the inner radiation belt (IRB) and SFT particles extend to outter radiation belt (ORB).

### 6.5. Source distributions

#### *6.5.1. Short flight time (SFT)*

The SFT particles are related to the bouncing motions between the northern and southern hemispheres, typically crossing the magnetic equator once ($N_b \lesssim 1/2$) or twice ($1/2 < N_b \lesssim 1$) (Huang 2000). Figure 15 shows two examples. The source and sink of SFT particles are near the magnetic footprints of the magnetic field lines at the detection sites; therefore they are distributed uniformly and show a similar pattern as the flight path of the shuttle. Figure 16 shows the source of SFT electrons and positrons.

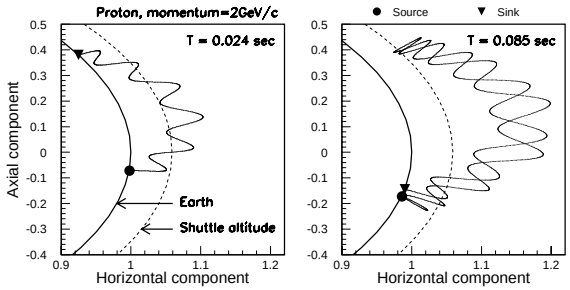


Fig. 15.— The typical trajectories of SFT particles are bouncing between the northern and southern hemisphere, their fight time are in the order of 1/2 (left figure) and 1 (right figure) bounce period.

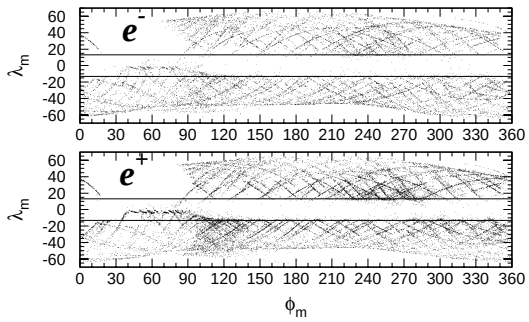


Fig. 16.— The source position of SFT particles in magnetic coordinates, where $\lambda_m$ is the magnetic latitude and $\phi_m$ is the magnetic longitude. The two lines mark the equaotrial gap at $|\lambda| = 13°$. The voids in the upper left corner are caused by the deletion of data taken when the AMS was inside the SAA region.

#### *6.5.2. Long flight time (LFT)*

The LFT particles are related to the longitudinal drift. Positive charged particles drift west-

ward, origin from the magnetic western hemisphere ($\phi_m = 180°$ to $360°$) and sink to the magnetic eastern hemisphere ($phi_m = 0°$ to $180°$). The typical drift times are $N_d \sim 1/4$ and $3/4$. Figure 17 shows the simplified trajectory of two examples. A few of the LFT events just drift $N_d \sim 1/8$ and do not cross $\phi_m = 180°$, these events are referred to as intermediate flight-time (IFT)events.

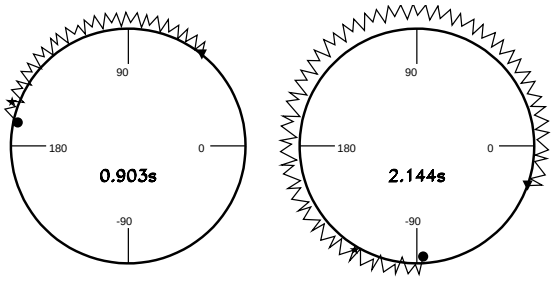


Fig. 17.— Two simplified trajectories of LFT particles viewed from North pole. The circle is the Earth and the azimuth angles is the geographic longitude. Only the mirroring points (which are near the Earth) and points when crossing the magnetic equator (which are away from the Earth and have highest altitude within $\tau_b/2$) are plotted. The LFT particles drift eastward/westward, their typical fight time are in the order of $1/4\tau_d$ (left figure) and $3/4\tau_d$ (right figure). The number shown in the center of the figure is the flight time in seconds.

The source (sink) position of these LFT particles concentrate in two regions around the SAA. Figure 18 shows the source of LFT electrons and positrons. Owing to the charge-time symmetry, the sinks of $e^+(e^-)$ are the sources $e^-(e^+)$. Albedo protons and helium have similar distribution as positrons.

LFT particles originate near $\phi_m = 0°$ where the surface magnetic fields are the weakest. Drifting away from the SAA, LFT particles encounter stronger magnetic field and mirroring at higher altitude. When they pass the $\phi_m = 180°$, the surface equatorial magnetic field are the strongest, the mirroring altitude decreases and finally intersects the atmosphere again. The source and sink are almost symmetric along $\phi_m = 0°$, however, the geomagnetic field is not just an offset dipole, the multipole moment produce two groups of LFT. The offset dipole will produce even distribution in

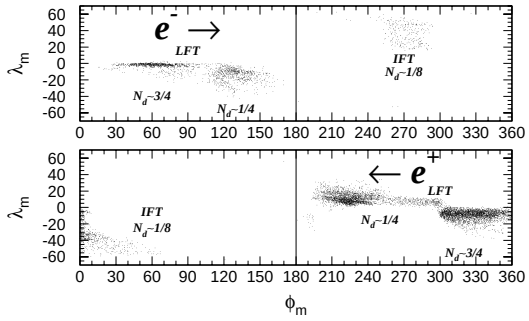


Fig. 18.— The source position of LFT particles in magentic coordinates. The arrows show the drift direction. The typical sources are concentrated in two areas near $\phi_m = 0°$. The IFT events are in $\phi_m < 180°$ for electrons and $\phi_m > 180°$ for positrons.

drift time distribution, unlike that shown in Figure 12.

The source position of electrons concentrate in two regions in the south magnetic hemisphere ($\lambda_m < 0$) and the source of positrons, protons and helium are in two regions on both sides of the magnetic equator. This is also caused by the multipole moment, which produces asymmetry in the magnetic field strength. The particles fall to the side where the magnetic field is weaker. However, the exact production sites are not only in the 40 km altitude, therefore, the exact source positions should be more dispersive.

### 6.6. Albedo positron electron ratio

The flux ratio of positrons to electrons varies with magnetic latitude and can be as large as 4 near the magnetic equator. Some balloon experiments, operated in high latitude regions, obtained a ratio of approximately 1. The excess of antimatter arouses questions concerning their origin. At high latitude, these albedo positrons could be higher than the cutoff and be mistaken as cosmic rays.

Owing to the geomagnetic rigidity cutoff, there are more cosmic rays coming from the west than from the east. This east-west effect is the major factor behind the large positron electron ratio. Because of the geomagnetic field, only the

positrons coming from the west and electrons coming from the east have the chance to move upward. Since the primary cosmic ray fluxes from the west are larger than those from the east, the secondary positrons from the west are more abundant than the electrons from the east. The difference in rigidity cutoff decreases with increasing magnetic latitude, so does the flux ratio.

A simple model was proposed to explain this large $e^+/e^-$ ratio, shown in Figure 19 (Huang 2000). Although this is just a first-order approximation, the quantitative agreements evidence the validity of this model.

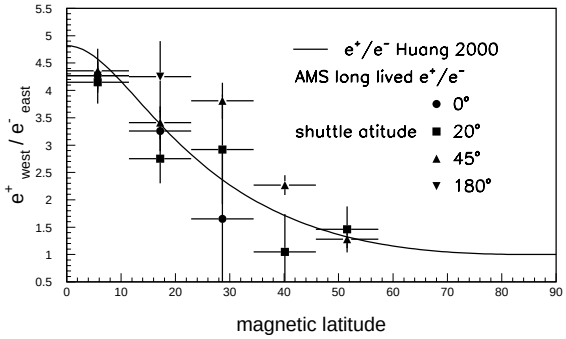


Fig. 19.— The AMS long flight-time $e^+/e^-$ can be explained by east-west effect.

### 6.7. Penumbra events

Events with $\tau_d/\tau_b < 15$ originate mostly in high latitude region or have high rigidity. Figure 20 shows some plots of these events. Their flight-time distributions do not have two distinct peaks, although the $N_b$ can still be used for classifying SFT and LFT. Some LFT particles can drift over several drift periods. This is the typical behaviors of the L-shell splitting at L-shell >4. Also, the rigidity of these events are inside the penumbra, their trajectories become irregular. The source of SFT particles is also uniformly distributed. However, the void in Fig. 6.5.1 does not appear in this figure. Unlike those in the Fig. 6.5.2, the sources of LFT particles spread over all longitudes. These penumbra events have different distributions. *The LFT penumbra events are not included in* (Alcaraz 2000B).

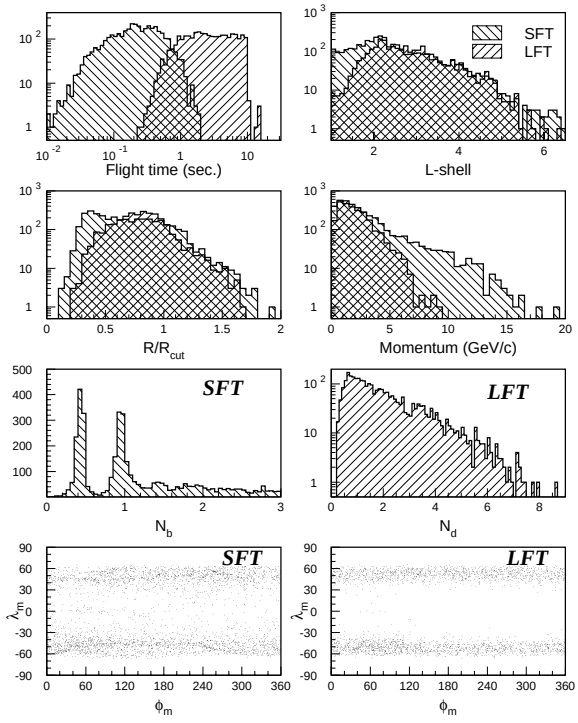


Fig. 20.— The various distributions of events with $\tau_d/\tau_b < 15$. These events originate mostly and are detected in high latitude and have rigidity close to the cutoff. Many of these particles can drift over one circle. Their source distributions are different from those of events with $\tau_d/\tau_b > 15$.

## 7. Summary

The physics results of the AMS01 shuttle flight are summarized as follows.

- Antimatter limit: $1.1 \times 10^{-6}$ for rigidity 1. to 140GV/c$^2$.
- Primary cosmic ray spectrum in 10GeV < R < 200GeV, $\Phi(R) = \Phi_0 R^{-\gamma}$ where $\Phi_0 = 17.1 \pm 2.0 \mathrm{GeV}^{2.78}/(\mathrm{m}^2\ \mathrm{s\ sr\ MeV})$ and $\gamma = 2.78 \pm 0.021$.
- Measurements of primary electrons and positrons are consistent with previous results.
- Many particles are discovered below the geomagnetic rigidity cutoff, these particle must

originate in the atmosphere and then rebound to space, i.e. atmospheric albedo particles.

- For particle well below the cutoff, two groups of atmospheric albedo particles are found, short flight-time and long flight-time particles.
  - Short flight-time particles are related to bounce motions, their sources are uniformly distributed, and they cover L-shell up to 6.
  - Long flight-time particles are related to longitudinal drift motions, their source/sink positions are distributed at two distinct areas at east/west of the magnetic prime-meridian ($\phi_m = 0°$), and they cover L-shell up to 4.
  - A large latitude-dependent albedo e+/e- ratio is discovered. A possible explanation is the east-west effect.
- Particles near the cutoff exist mostly in high latitude and could drift over several drift periods. Their source distributions are different from those of particles well below cutoff.

The author wishes to thank the organizer of this workshop, Professor C.M. Ko for his kind invitation. This study was supported by grant NSC89-2811-M-001-0076 from the National Science Council, Taiwan, ROC.

## REFERENCES

[1]Agrinier, B. et al., 1969, Lett. Nuovo Cimento, 1, 153

[2]Aharonin, F.A. & Atoyan, A.M. 1995, J. Phys. G, 17 1769

[3]Ahlen, S. et al. 1994, Nucl. Inst. Meth A, 419, 295

[4]Aizu, H. et al. 1961, Phys. Rev., 121, 1206

[5]Alcaraz, J. et al. 1999, Phys. Lett. B, 461, 387

[6]Alcaraz, J. et al. 2000 A, Phys. Lett. B, 472, 215

[7]Alcaraz, J. et al. 2000 B, Phys. Lett. B, 484, 10

[8]Alcaraz, J. et al. 2000 C, Phys. Lett. B, 490, 27

[9]Barbiellini, G. et al. 1996, A&A, 309, L15

[10]Badhwar, G.D. et al. 1978, Nature, 274, 137

[11]Barwick, S.W. et al. 1995 Phys.Rev.Lett., 75, 390

[12]Barwick, S.W. et al., 1998, J. Geophys. Res. 103, 4817

[13]Bleeker, J.A.M. et al. 1965, Proc. 9th Int. Cosmic Ray Conf., (London), 7, 723

[14]Boezio, M. et al. 1999, ApJ, 518, 457

[15]Buffington , A. et al. 1975, ApJ, 199, 669

[16]Buffington, A. et al. 1981, ApJ, 248, 1179

[17]Clem, J. et al. 1995, Proc. 24th Int. Cosmic Ray Conf., (Rome), 3, 5

[18]Daugherty, J. K. et al. 1975, ApJ, 198, 493

[19]Dogiel, V.A., & Sharov, G.S. 1990, A&A,229, 259

[20]Evenson, P. 1972, ApJ, 176, 797

[21]Fanselow, J.L. et al. 1969, ApJ, 158, 771

[22]Gaisser, T.K. 1999, Nucl. Phys. Proc. Suppl.77, 133

[23]Galper, A.M. et al. 1983, Proc. 18th Int. Cosmic Ray Conf., (Bangalore), MG10-33, 497

[24]Golden, R.L. et al. 1987, A&A 188, 145

[25]Golden, R.L. et al. 1994, ApJ 436, 769

[26]Golden, R.L. et al. 1996, ApJ 457, 103

[27]Golden, R.L. et al. 1997, ApJ 479, 992

[28]Gustafsson, G., N. E. Papitashvili, and V. O. Papitashvili 1992, J. Atmos. Terr. Phys. 54, 1609

[29]Harding, A. K., & Ramaty, R. 1987, Proc. 20th Int. Cosmic Ray Conf. (Moscow), 2, 92

[30]Hovestadt, D., Meyer, P., & Schmidt, P.J., 1971, Astrophys. Lett., 9, 165

[31]Honda, M. et al. 1995, Phys.Rev.D, 52, 4985

[32]Huang, M.A. et al. 2000, in the 8th Asia Pacific Physics Conference (Taipei), (to be published by World Scientific); astro-ph/0009106

[33]Huang, M.A., et al. 2001, Chinese Journal of Physics, 39, 1

[34]Israel, M.H. 1967, J. Geophys. Res., 72, 4701

[35]Just, L. et al. 1983, J. Geophys. 52, 247

[36]Kamionkowski, M., & Turner, M.S. 1991, Phys.Rev.D, 43, 1774

[37]Menn, W. et al. 2000, ApJ, 533, 281

[38]Muller D. & Tang, K.K., 1987, ApJ, 312, 183

[39]Rockstroh, J. & Webber, W.R. 1969, J. Geophys. Res.,74, 5041

[40]Saeki, T. et al., 1998, Phys. Lett. B, 422, 319

[41]Sanuki, T. et al. 2000, astro-ph/0002481

[42]Schmoker, J.W. & Earl, J.A. 1965, Phys. Rev., 138, 300

[43]Smoot, G.F., Buffington, A.,& Orth, C.D., 1975, Phys.Rev.Lett., 35, 258

[44]Stephens, S.A. 1970, Acta Phys. Hung., 29 suppl. 727

[45]Strömer, C. 1930, Astrophysics, 1, 237

[46]Turner, M.S., & Wilczek, F. 1990, Phys.Rev.D, 42, 1001

[47]Tylka, A.J., 1989, Phys.Rev.Lett., 63, 840

[48]Verma,S.D. 1967, J. Geophys. Res., 72, 915

[49]Verma,S.D. & Bhatnagar, S.D. 1985, Proc. 19th Int. Cosmic Ray Conf. (La Jolla), SH, 316

[50]Walt , M. 1994, "Introduction to geomagnetically trapped radiation", (Cambridge University Press)